

Simulation on biomarker sensor miniaturization based on metamaterial

Ruitao Liu* and Tianhong Cui^{†,‡}

**Department of Precision Instruments,
Tsinghua University, Haidian, Beijing, China*

[†]*Department of Mechanical Engineering,
University of Minnesota, Minneapolis, MN 55455, USA*

[‡]*cui@tc.umn.edu*

Received 18 September 2018

Accepted 12 February 2019

Published 1 April 2019

Cancer is always the greatest threat to human health. In this work, a split-ring resonator (SRR)-based sensor was simulated for label-free detection on biomarkers in microwave. The model of biosensor was simulated by Computer Simulation Technology 2017 (CST2017) and some influences of feature parameters on resonance frequency and Q -factor were also discussed. From the simulation results, the model of sensor in our work showed ultrahigh Q -factor and sensitivity under different permittivities and also exhibited a trend of better performance when it works in higher frequency. Therefore, the SRR-based biosensor will become an important application in cancer precaution and treatment in the future.

Keywords: SRR; biomarker detector; metamaterial; CST simulation.

1. Introduction

Health of human beings is always one of the hottest topics. Cancer, as the biggest threat, has taken more and more attention. In the last century, some worldwide cancer research centers had been built, including the famous International Agency for Research on Cancer (IARC). According to the statistics of these institutions,^{1,2} among the various kinds of cancer, the incidence rate of prostate cancer is the highest (almost 80%) in Western adult males.

In recent years, although many new methods to detect biomarkers had been found, device miniaturization became a new direction of research. The miniaturized sensors should not only have ultrahigh detection accuracy and sensitivity, but also show higher adaptability to complex detection environment, so it is of great significance for cancer early diagnosis and treatment. However, due to increasing

[‡]Corresponding author.

requirements for the miniaturized sensors, the characteristics of high throughput (HTP), ultrahigh sensitivity and ultralow detection limit (LoD) are needed urgently on the basis of existing researches. In order to improve the sensitivity and accuracy of these miniaturization sensors, some researchers³⁻⁷ decorate the secondary markers (Ab2) with modern materials or microstructure, such as carbon nanotube (CNT), nanoparticles (NPs) and so on. Sharafeldin *et al.*⁸ demonstrated an electrochemical-based biosensor by using magnetic Fe₃O₄/GO composites as the second marker such that Fe₃O₄ NP provided the precise number control for each GO sheet, and optimized the dynamic range of the sensor. As a second marker, silver-enhanced Au NPs will change the photocurrent of OPDs under the different concentrations of biomarker. Dong and Pires⁹ described an optical microfluidic biosensor with polythiophene: PC70BM BHJ OPDs. Chuang *et al.*¹⁰ developed a TNF- α detection sensor by measuring different diffusivities, which immobilizes biomarker with Au NPs onto the surface of particles. Zhao *et al.*¹¹ demonstrated a new method to control the amplification strategy by changing the thickness of shell upon the Au NPs, which optimizes the detection sensitivity for CEA and AFP. Zou *et al.*¹² reported the development of a metal-ion-dependent DNAzyme recycling signal enchantment strategy for sensitive and homogeneous immuno-proximity binding assay of protein biomarkers. Compared with traditional detection devices, these new methods optimize the performance of detection to some extent. However, these second marker-based sensors are always limited because of complicated pretreatment process and much more detection requirements (like POC, etc.). Therefore, more and more researchers transferred their attentions upon the label-free biomarker sensors.

Compared with the label-based biomarker sensor, label-free sensors can be used in more complex detection environment because they do not need the complex secondary antibody decoration to biomarkers. Myung *et al.*¹³ demonstrated a novel strategy for the fabrication and application of a reduced graphene oxide (rGO)-encapsulated NP-based FET biosensor for HER2 and EGFR detection, which improved the LoD by increasing the surface-to-volume ratio. Zhang *et al.*¹⁴ fabricated a layer-by-layer graphene nanosheet to detect PSA. In their work, the sensitivity of the sensor can be improved by using the high-electron-mobility substrate and the background noise is effectively suppressed due to the suspended structure, moreover, the double-sided structure can effectively increase the capture efficiency and amplify the relative conductivity changes. The LoD of sensor is 0.4 fg/mL for PSA. Gao *et al.*¹⁵ developed a standard nanowire-based biosensor for multiplexed detection of lung cancer biomarkers, which is fabricated by CMOS technologies. Although these miniaturized label-free sensors have achieved ultralow detection limits and high sensitivity, they are still difficult to maintain the stability because the microstructures fabrication technology and material growth are not well reliable in industry.

In order to solve these problems, a Korea research group¹⁶⁻¹⁸ designed and fabricated a series of sensors with split-ring resonator (SRR) structure which is a kind of metamaterial. By measuring frequency shifts in S_{11} (or S_{21}) parameters, PSA

and some other biomarkers with different concentrations will be detected. Besides, many more scientists fabricated metamaterial-based sensors to detect more biological information on human bodies. Camli *et al.*¹⁹ fabricated a split-ring resonator on an FR-4 substrate by PCB fabrication techniques to detect glucose concentration. Saxena and Daya²⁰ presented the simulation results and theoretical model of the sensing property of concentric square ring metamaterial biological materials by CST MWS software. Ahmadvand *et al.*²¹ introduced a THz metasensor based on a plasmonic surface consisting of metamolecules and demonstrated the detection of an ultralow concentration targeted biomarker. Ekinici *et al.*²² fabricated SRR-based strain sensor for glaucoma detection, which was realized on flexible substrates and could be embedded in the conventional contact lens. Due to the developments in microfabrication, some researchers fabricate metasensors of nanometer size with the resonance frequency in the THz range. Geng *et al.*²³ fabricated two kinds of THz metamaterials biosensor integrated with microfluidics which overcame water absorption and enhanced the THz biosensing sensitivity.

In this work, an SRR-based biosensor with microsize was designed and simulated by CST 2017 software to study the influences of sensor miniaturization on the detection accuracy and sensitivity which has already become a key point in metadvice research. Due to the lower power losses (including radiation loss and Ohmic loss), the SRR-based microwave biosensor provides ultrahigh Q -factor for permittivity detection. Compared with previous works, not only some influences of feature sizes of SRR structure on resonance frequency and Q -factor were discussed, but also some influences of sensor miniaturization on the accuracy and sensitivity of permittivity detection were investigated in a deep level. According to the simulation result, the miniaturized sensor will work in terahertz range and achieve better performances (such as LoD, sensitivity, accuracy, etc.) in the future.

2. Materials and Methods

2.1. Metamaterials

Metamaterial is a “material” artificially engineered to have a property that is not found in nature,²⁴ which is always assembled by multiple individual periodical metal arrays in microfabrication.²⁵ Since these metallic units are much less than a wavelength of incident electromagnetic wave in size, the periodic array structure is considered as the homogeneous material and the properties depend on artificial structure rather than the materials themselves. Microstructures array such as SRR is capable of manipulating electromagnetic wave, hence these kinds of metamaterials are widely used in many fields, such as antennas, superlens, cloaking devices and electromagnetic wave filters.

2.2. Module of SRR structure and the boundary condition

As Fig. 1 shows, there are many types of SRR structures and different structures always have different characteristics in resonance frequency. For example, some

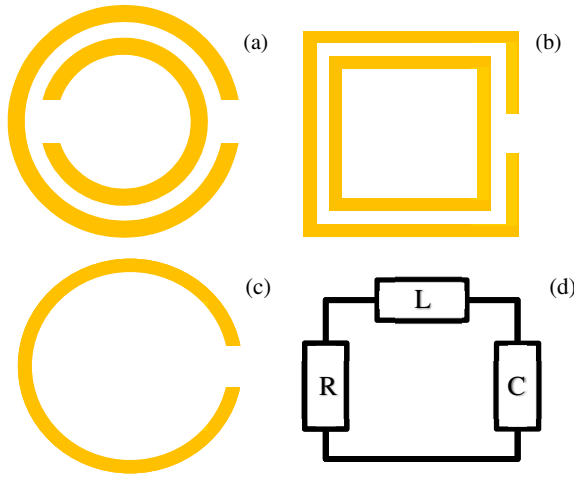


Fig. 1. Schematic diagram of the basic SRR structure and the equivalent circuit. (a) Double-circle SRR, (b) double-rectangle SRR structure, (c) single-circle SRR structure and (d) the equivalent circuit of SRR structure.

researchers²⁶ tried to widen the frequency band by fabricating a sectional asymmetric structure and successfully designed a band-stop filter, while some other researchers²⁷ tried their best to narrow the bandwidth to achieve higher Q -factor and improved the accuracy of their detectors. Anyway, the SRR structure can be modeled into a classic LRC oscillating circuit, as shown in Fig. 1(d), and the resonance frequency (ω_0) is given by the following equation^{28,29}:

$$\omega_0 = 2\pi f_0 = \frac{K}{\sqrt{LC}}, \quad (1)$$

where L and C are equivalent inductance and capacitance decided by the dimensions of the SRR. When we fabricate the SRR into millimeter scale, the resonance frequency of the sensor is always in the range of GHz. As the width of ring decreases, L and C values will decrease simultaneously, and resonance frequency will increase sharply. In the last few years, scientists had put their attentions upon visible light-invoked devices and THz electromagnetic waves by designing the SRR structure in tens of nm scale, and then some novel sensors have been fabricated with ultrahigh performance.

As Fig. 2 shows, we design a model of double-rectangular SRR structure by simulation using CST 2017. The SRR is made from gold and the substrate is Si ($\epsilon_r = 11.9$), the widths of both rings and splits are $100 \mu\text{m}$, the thickness of SRR is $5 \mu\text{m}$. Sides of the cell have ports, left port is input port (Port 1) and right port is output port (Port 2), respectively. We set the boundary condition as shown in Fig. 2(b) which will save the simulation time effectively due to the symmetry of electric field or magnetic field in specified directions of the cell. The directions of electric field and magnetic field are y -axis and x -axis, respectively, which could couple with SRR structure by magnetic resonance.

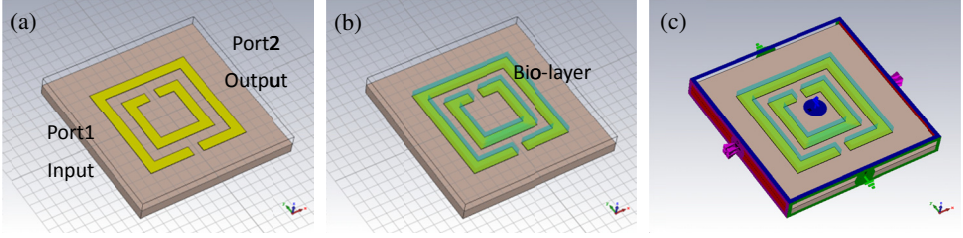


Fig. 2. Simulation model of SRR. The 3D model and ports are marked in (a), (b) is the 3D model with biolayer and (c) shows the boundary condition.

2.3. Mechanism of biomarker detection

As mentioned above, SRR-based sensor can be viewed as a filter which only blocks the transmission of electromagnetic wave at its resonance frequency. However, the resonance frequency depends on various factors, such as the feature sizes of SRR, the permittivities of substrate and SRR and so on. Therefore, the S -parameter will show the frequency shift of sensor when the feature sizes or permittivities change. If we immobilized biomarkers onto the surface of SRR, the total permittivity of SRR will be changed, and then the frequency will shift and the more the capturing biomarkers the bigger will be the shift.

3. Results and Discussion

3.1. Influence of sensor miniaturization on the detection accuracy

As we know, the resonance frequency of SRR-based sensor will show the concentration of biomarker and detection accuracy depends on the Q -factor, i.e. detection accuracy will increase as the Q -factor increases. Therefore, we design and build two models: one is only the SRR as Fig. 2(a) shows and the other one is an SRR with biolayer as Fig. 2(b) shows, and we conduct high-frequency electromagnetic wave simulation to analyze the power losses and Q -factor. In this simulation experiment, the side length is $1000 \mu\text{m}$ and permittivity values of biolayer are in the range of 1–8.

As Fig. 3(a) shows, the sum of power losses includes surface loss and volume loss, and volume loss plays the major role. In this group of simulations, we simulate the frequency from 15 GHz to 25 GHz and sum of power losses is in the range of 2.6–4.22 mW and Q -factor is in the range of 312.15–387.09. These discrete data are fitted by a second-stage polynomial [as Figs. 3(a) and 3(b) show] and the fitting functions of sum of Q -factors and sum of power losses can be obtained as follows:

$$f_Q(x) = -1.75293x^2 + 75.24293x - 419.86455,$$

$$f_{\text{Power loss}}(x) = 3.8 \times 10^{-5}x^2 - 0.00142x + 0.01578.$$

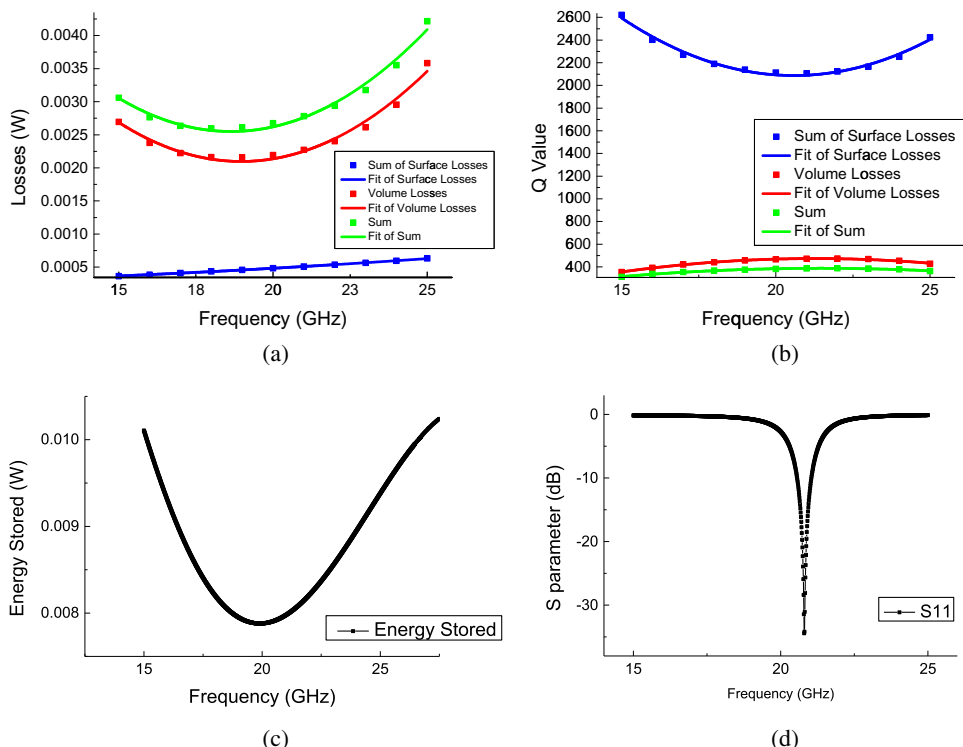


Fig. 3. (Color online) Simulation results of power losses and Q -factor without biolayer. (a) shows the power loss, (b) shows the Q -factor, (c) shows the calculated energy stored and (d) shows the S_{11} transport line of the SRR unit.

According to the basic meaning of Q -factor which represents the energy stored from the energy dissipated per cycle of the sensor, therefore, it can be represented as follows:

$$Q = 2\pi \times \frac{\text{Energy stored}}{\text{Energy dissipated per cycle}} = 2\pi f_r \times \frac{\text{Energy stored}}{\text{Power loss}}.$$

By simplifying and calculating the fitting function, the stored energy can be obtained in Fig. 3(c). By analyzing the simulation results from Figs. 3(a)–3(c), a minimum point can be found which means the lowest stored energy at that frequency point — resonance frequency. Therefore, the electromagnetic wave will not be blocked at resonance frequency, which matches with the simulation result of S -parameter [shown in Fig. 3(d)].

From the investigation of the present work about SRR power losses, the structure which was shown in Fig. 2(a) provides certain suppression of radiation loss due to the reverse electric dipole model and working in the microwave frequency. Therefore, the main factor affecting the Q -factor is Ohmic loss. We simulate SRR with biolayer model which is shown in Fig. 2(b). In this simulation, the biolayer with different permittivities represents different concentrations of biomarker. Analyzing

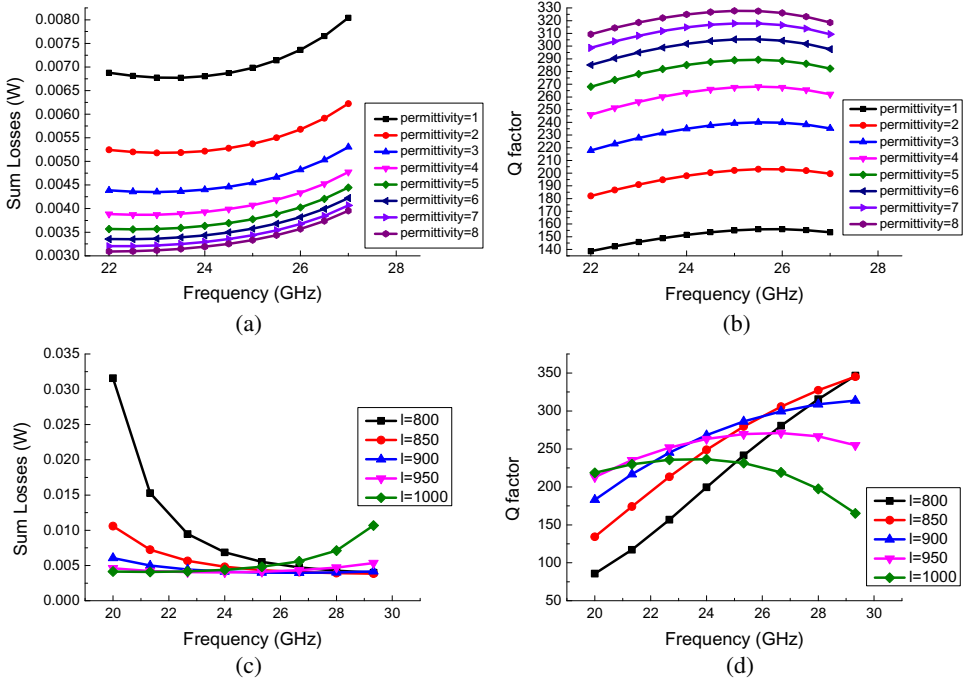


Fig. 4. (Color online) Simulation results of power losses and Q -factor with biolayer. (a) shows the power losses with different permittivities, (b) shows the Q -factors with different permittivities, (c) shows the power losses with different side lengths and (d) shows the Q -factors with different side lengths (permittivity = 7).

these simulation results which are shown in Figs. 4(a) and 4(b), we can achieve the same trends of power loss and Q -factor between the two models [shown in Figs. 2(a) and 2(b)]. As permittivity of biolayer increases, the power loss decreases and Q -factor increases, but these changes tend to be slow. Therefore, the SRR-based sensor will have better accuracy when detecting the permittivity changes at a greater value. As Figs. 4(c) and 4(d) show, SRRs with different side lengths are simulated, the peak value of Q -factor shows a certain increase as the SRR shrinks and the detailed data are collected as shown in Fig. 5. Through the statistics of the simulation results, when a larger permittivity is detected, the miniaturization sensor has a greater influence on the Q -factor and better detection accuracy.

3.2. Influence of sensor miniaturization on the sensitivity

3.2.1. Influence of widths of the split on the S -parameter

In this simulation experiment, we try to design different widths of split from $50 \mu\text{m}$ to $250 \mu\text{m}$. Under the different feature sizes, resonance frequency will change in our simulation model, and the simulation results are shown in Fig. 6.

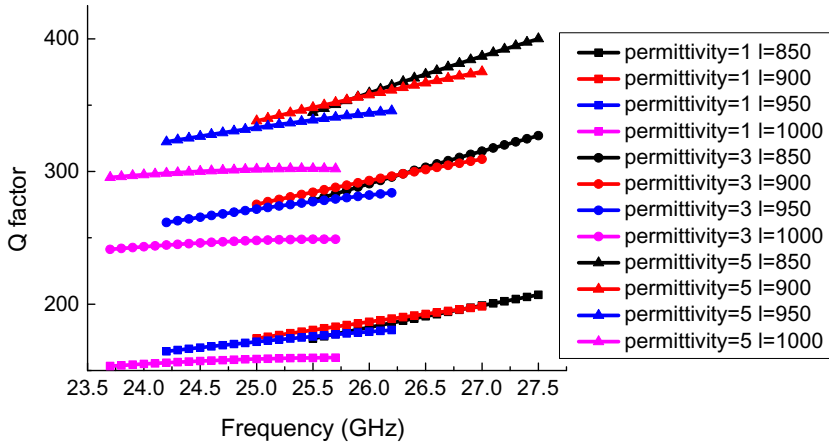


Fig. 5. (Color online) Simulation results of Q -factor with different side lengths and different permittivities. Same marker represents the same permittivity of bi-layer, and the same color means the same side length.

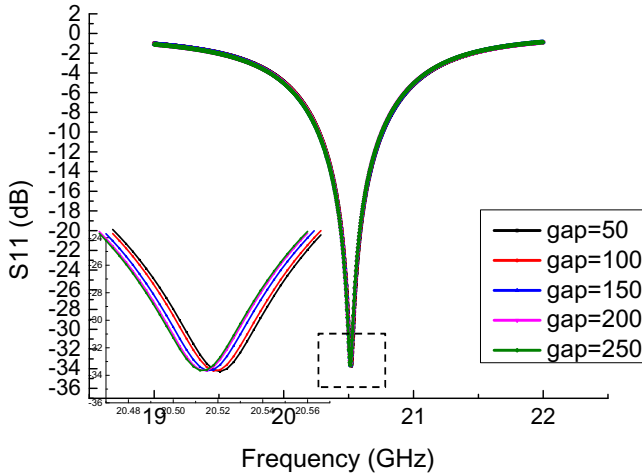


Fig. 6. (Color online) S_{11} -parameter variations with different widths of split. Different widths of split were marked with different colors.

When this SRR sensor works at resonance frequency, the intensity of electromagnetic field of the input is measured by the SRR structure and exhibited as a trough of wave. In this group of simulations, we scan the frequency from 19 GHz to 22 GHz and the S_{11} variations are shown in Fig. 5. While measuring and calculating these S -parameters, the resonance frequency increases as we extend the split, because when the split width becomes larger, the equivalent inductance (L) has little changes, but equivalent capacitance (C) will decrease obviously, and LC will decrease simultaneously. According to Eq. (1), the resonance frequency will increase with the decrease of LC .

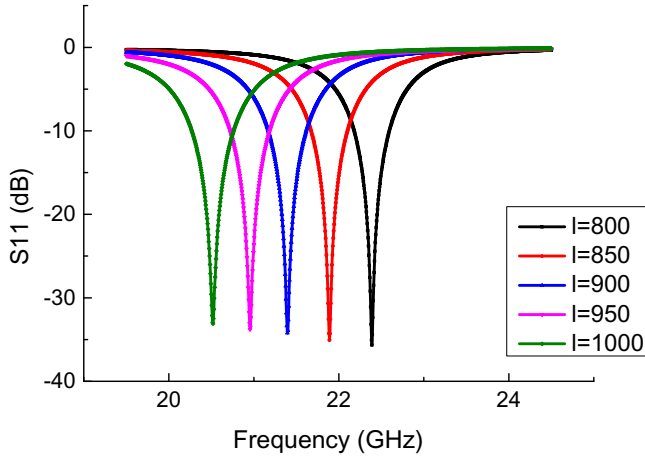


Fig. 7. (Color online) S_{11} -parameter variations with different lengths of side which are marked with different colors.

3.2.2. Influence of side length on the S -parameter

In this simulation experiment, we have designed different lengths of the side from $800 \mu\text{m}$ to $1000 \mu\text{m}$. The simulation results are shown in Fig. 7.

According to the simulation results from Fig. 7, as the sensor works from 20.5 GHz to 22.5 GHz , there is an obvious increase in the resonance frequency as the side length decreases. Due to the miniaturization of the sensor, the smaller ring will reduce the values of equivalent capacitance and inductance simultaneously which produces a blue frequency shift in S -parameter.

3.2.3. Influence of different permittivities of biolayer on the S -parameter

As we know, the permittivity will change little after the combination of antibody and antigen due to different permittivity values between them, which could be easily detected by the SRR-based biomarker sensor. In this simulation, we design another layer attached onto the surface of gold layer [as shown in Fig. 2(b)] and simulate as the biomarker by setting its permittivity from 1 to 8.

As shown in Fig. 8, a red resonance frequency shift was produced with the increase of permittivity which represents higher concentration of biomarker. When we detect biomarkers in higher concentration, more biomarkers will be captured by the specific binding between antibody and antigen, which means much more capacitances in series to SRR, increase in the total equivalent capacitance and reduction of resonance frequency of the sensor. Besides, we also simulate the S -parameters under different side lengths to calculate the sensitivity due to the miniaturization of the sensor (as shown in Fig. 9).

As shown in Fig. 9, the resonance frequency reduces as the permittivity increases which matches with the simulation results from Fig. 8, and a big change of resonance

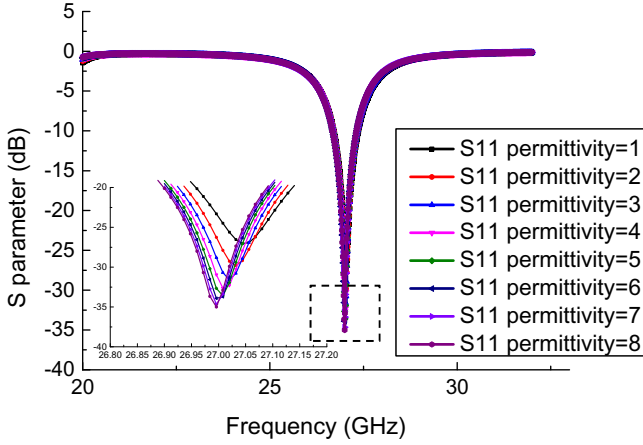


Fig. 8. (Color online) Simulation of SRR with biomarker layer.

Table 1. Resonance frequencies by Lorentz fitting with different permittivities and side lengths.

Side length (μm)	Resonance frequency (GHz)					Average Δf (GHz)
	$\epsilon = 1$	$\epsilon = 2$	$\epsilon = 3$	$\epsilon = 4$	$\epsilon = 5$	
$l = 800$	27.04727	27.0314	27.02023	27.01215	27.00607	0.0103
$l = 850$	26.43192	26.41577	26.4043	26.39601	26.38976	0.01054
$l = 900$	25.82455	25.80865	25.79729	25.78904	25.78281	0.010435
$l = 950$	25.27803	25.26157	25.24975	25.24116	25.2347	0.010833
$l = 1000$	24.73654	24.72022	24.7084	24.69978	24.69328	0.010815

frequency happens when using the sensor with different sizes. In this simulation, we fit these discrete points by using Lorentz fitting equation and calculate resonance frequency as shown in Table 1.

As shown in Table 1, the average frequency differences change a little among different side lengths. The SRR sensor does not show better performance in detection sensitivity with the decrease of sizes. As it is analyzed previously, the equivalent capacitance plays a major role on resonance frequency compared to equivalent inductance. In fact, the total equivalent capacitance of standard SRR structure includes many parts, such as splits gap, rings gap and surfaces gap, and the capacitance of rings gap dominates the total equivalent capacitance at large size. With the shrink of sensor size, the capacitance of splits gap plays an enhanced role on the total equivalent capacitance. According to the basic principle of parallel plate capacitance, shortening the side length does not affect the capacitance generated by the inner and outer rings, but the capacitance of splits gap becomes smaller, which leads to a decrease in the slope of the sensor to the dielectric constant, and thus the detection sensitivity slightly decreases.

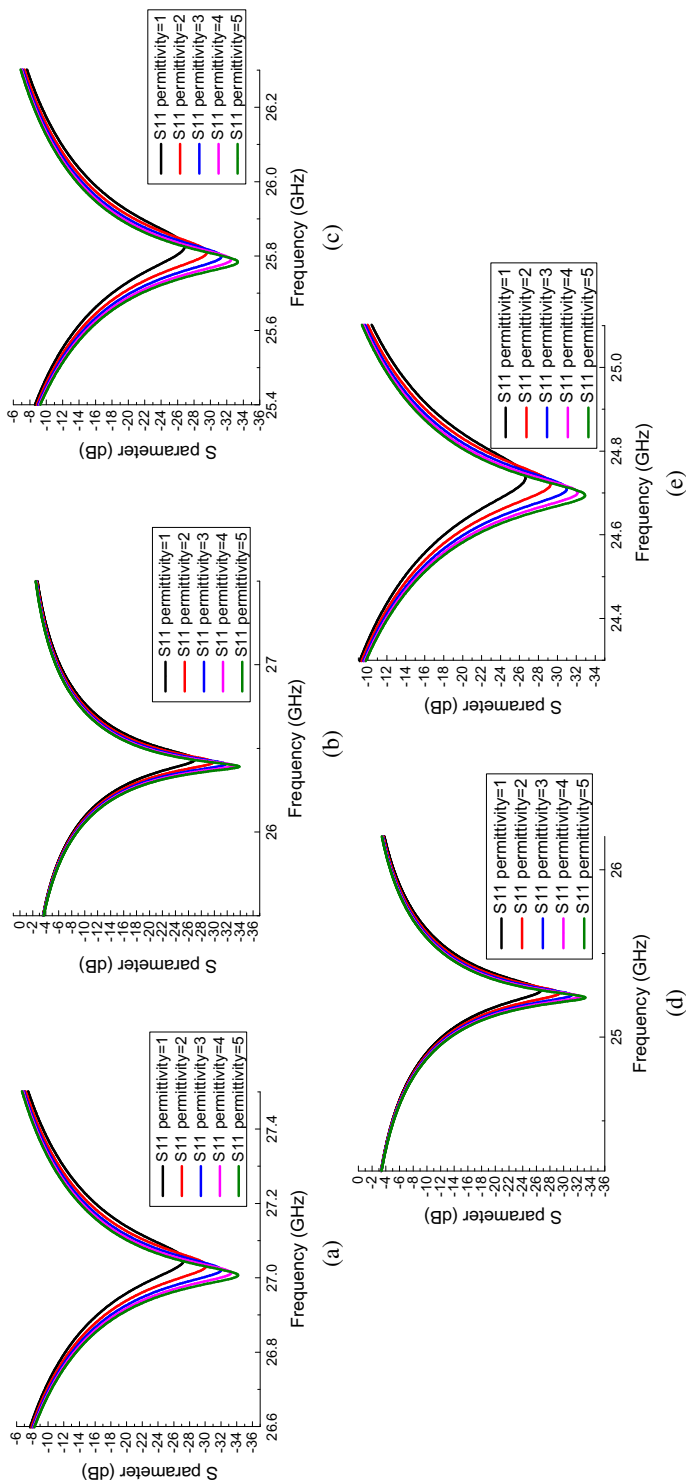


Fig. 9. (Color online) Resonance frequencies with different permittivities and different side lengths. The permittivities are from 1 to 5 with different colors, and the sides lengths of (a)–(e) are 800, 850, 900, 950 and 1000 μm, respectively.

4. Conclusion

Metamaterial is a novel kind of material and has attracted many scientists' attentions in the recent years due to its performance beyond the limitation of traditional materials. Some of them have been investigated and fabricated as wave filters, clocking devices and absorbers because they can control both energy and direction of propagation by controlling the artificial structures. SRR is a kind of metamaterial which may be the most easy to realize, as it always works at ultrahigh frequency and has high Q -factor, the SRR-based metadevices are always used in biomedical and communication fields.

As the SRR-based biosensor works in ultrahigh frequency, there are some benefits: first, when the sensors work at a higher resonance frequency they will achieve a higher Q -factor due to the reduction of Ohmic loss; second, the sensors with ultrahigh resonance frequency will undergo larger frequency changes when under the same concentration conditions, hence they will improve the sensitivity and detection limits of these sensors; finally, according to the relationship between the frequency and wavelength of electromagnetic waves, which within the range of tens to hundreds of THz can be more easily produced, if we expand the frequency bandwidth to thousands of THz, the SRR structure will be driven by the visible lights, which is of significant advantage for metamaterial devices in the research field.

In this work, we design an SRR-based model in microlevel and simulate the resonance frequency shifts under different feature sizes and permittivities, which offers us important experience and guidance when designing the SRR structure in the future. By analyzing the simulation results, we not only explain the basic principle of SRR-based biosensor, but also exhibit a trend of better performance of the SRR-based biosensor when it continues to be downsized. With the decrease in size of standard SRR-based sensor, the detection accuracy will increase but sensitivity has no significant change. Therefore, a metamaterial with a new structure should be studied in the future to improve the sensitivity of dielectric constant detection with sensor miniaturization. Based on the study in this work, we have ample reason to believe the SRR-based biosensor will be widely used in real-time and for early cancer detection in the future because of its advantages including ultrahigh sensitivity, accuracy and low cost.

Acknowledgments

This work was partially supported by the State Key Laboratory of Precision Measurement Technology and Instruments, Tsinghua University, China.

References

1. M. M. Center *et al.*, *Eur. Urol.* **61** (2012) 1079.
2. J. Ferlay *et al.*, *Int. J. Cancer* **136** (2015) E359.
3. N. P. Sardesai, K. Kadimisetty, R. Faria and J. F. Rusling, *Anal. Bioanal. Chem.* **405** (2013) 3831.

4. S. Krishnan, V. Mani, D. Wasalathanthri, C. V. Kumar and J. F. Rusling, *Angew. Chem. Int. Ed.* **50** (2011) 1175.
5. B. V. Chikkaveeraiah, V. Mani, V. Patel, J. S. Gutkind and J. F. Rusling, *Biosens. Bioelectron.* **26** (2011) 4477.
6. G. Jie *et al.*, *Anal. Chem.* **80** (2008) 4033.
7. S. I. Stoeva, J. S. Lee, J. E. Smith, S. T. Rosen and C. A. Mirkin, *J. Am. Chem. Soc.* **128** (2006) 8378.
8. M. Sharafeldin *et al.*, *Biosens. Bioelectron.* **91** (2017) 359.
9. T. Dong and N. M. M. Pires, *Biosens. Bioelectron.* **94** (2017) 321.
10. H. S. Chuang, Y. J. Chen and H. P. Cheng, *Biosens. Bioelectron.* **101** (2018) 75.
11. Y. Zhao *et al.*, *Biosens. Bioelectron.* **99** (2018) 193.
12. M. Zou, D. Li, R. Yuan and Y. Xiang, *Biosens. Bioelectron.* **92** (2017) 624.
13. S. Myung *et al.*, *Adv. Mater.* **23** (2011) 2221.
14. B. Zhang, Q. Li and T. Cui, *Biosens. Bioelectron.* **31** (2012) 105.
15. A. Gao *et al.*, *Biosens. Bioelectron.* **91** (2017) 482.
16. H. J. Lee *et al.*, *Sens. Actuators B-Chem.* **169** (2012) 26.
17. H. J. Lee, J. H. Lee and H. I. Jung, *Appl. Phys. Lett.* **99** (2011) 163701.
18. H. J. Lee *et al.*, *Appl. Phys. Lett.* **103** (2013) 053702.
19. B. Camli *et al.*, *IEEE J. Sel. Top. Quant. Electron.* **23** (2017) 6900706.
20. K. Saxena and K. S. Daya, *Integr. Ferroelectr.* **184** (2017) 50.
21. A. Ahmadivand *et al.*, *Biomed. Opt. Express* **9** (2018) 373.
22. G. Ekinci *et al.*, *Sens. Actuators A-Phys.* **268** (2017) 32.
23. Z. Geng, X. Zhang, Z. Fan, X. Lv and H. Chen, *Sci. Rep.* **7** (2017) 16378.
24. H. Caglayan *et al.*, *Appl. Phys. Lett.* **97** (2010) 2075.
25. T. Chen, S. Li and H. Sun, *Sensors* **12** (2012) 2742.
26. C. Gong *et al.*, *Sci. Rep.* **6** (2016) 32466.
27. Z. Geng, X. Guo, Y. Cao, Y. Yang and H. Chen, *Microelectron. Eng.* **135** (2015) 23.
28. D. R. Smith, J. B. Pendry and M. C. K. Wiltshire, *Science* **305** (2004) 788.
29. S. RoyChoudhury, V. Rawat, A. H. Jalal, S. N. Kale and S. Bhansali, *Biosens. Bioelectron.* **86** (2016) 595.